Magnetic anisotropy and GGG substrate stray field in YIG films down to millikelvin temperatures

Check for updates

Rostyslav O. Serha[1,2] ✉, Andrey A. Voronov[1,2], David Schmoll[1,2], Roman Verba[3], Khrystyna O. Levchenko[1], Sabri Koraltan[1,2,4], Kristýna Davídková[1,2], Barbora Budinská[1,2], Qi Wang[5], Oleksandr V. Dobrovolskiy[1], Michal Urbánek[6], Morris Lindner[7], Timmy Reimann[7], Carsten Dubs[7], Carlos Gonzalez-Ballestero[8], Claas Abert[1,4], Dieter Suess[1,4], Dmytro A. Bozhko[9], Sebastian Knauer[1] & Andrii V. Chumak[1]

Quantum magnonics investigates the quantum-mechanical properties of magnons, such as quantum coherence or entanglement for solid-state quantum information technologies at the nanoscale. The most promising material for quantum magnonics is the ferrimagnetic yttrium iron garnet (YIG), which hosts magnons with the longest lifetimes. YIG films of the highest quality are grown on a paramagnetic gadolinium gallium garnet (GGG) substrate. The literature has reported that ferromagnetic resonance (FMR) frequencies of YIG/GGG decrease at temperatures below 50 K despite the increase in YIG magnetization. We investigated a 97 nm-thick YIG film grown on 500 µm-thick GGG substrate through a series of experiments conducted at temperatures as low as 30 mK, and using both analytical and numerical methods. Our findings suggest that the primary factor contributing to the FMR frequency shift is the stray magnetic field created by the partially magnetized GGG substrate. This stray field is antiparallel to the applied external field and is highly inhomogeneous, reaching up to 40 mT in the center of the sample. At temperatures below 500 mK, the GGG field exhibits a saturation that cannot be described by the standard Brillouin function for a paramagnet. Including the calculated GGG field in the analysis of the FMR frequency versus temperature dependence allowed the determination of the cubic and uniaxial anisotropies. We find that the total crystallographic anisotropy increases more than three times with the decrease in temperature down to 2 K. Our findings enable accurate predictions of the YIG/GGG magnetic systems behavior at low and ultralow millikelvin temperatures, crucial for developing quantum magnonic devices.

Magnonics is the field of science that deals with data carried and processed by spin waves and their quanta, magnons, in magnetically ordered media[1]. The ferrimagnet yttrium iron garnet (YIG) $Y_3Fe_5O_{12}$ is the material with the lowest known magnetic damping as bulk material[2–4] and in the form of thin films[5–11]. Thus, YIG is the medium with the longest propagation lengths and lifetimes, in which magnons exist up to one microsecond[12]. Therefore, YIG has emerged as a preeminent material in RF technologies and magnonic experiments, showing promise for quantum magnonic applications. The field of quantum magnonics is a rapidly growing and highly promising research area that operates with quantum magnonic states, e.g. single magnons, and hybrid structures[1,13–21]. These investigations have to be performed at millikelvin temperatures to ensure that there is minimal thermal noise, allowing for precise observation and manipulation of the quantum states of magnons, which are extremely fragile to any kind of distortion.

Note, YIG was already the material of choice in experiments at low kelvin and ultralow millikelvin temperature magnonics for coupling to superconducting resonators[13,18,22,23] and propagating spin-wave spectroscopy[19,24,25]. Furthermore, the first demonstration of magnon control and detection at the

[1]Faculty of Physics, University of Vienna, 1090 Vienna, Austria. [2]Vienna Doctoral School in Physics, University of Vienna, 1090 Vienna, Austria. [3]Institute of Magnetism, Kyiv 03142, Ukraine. [4]Research Platform MMM Mathematics - Magnetism - Materials, University of Vienna, Vienna, Austria. [5]Huazhong University of Science and Technology, Wuhan, China. [6]CEITEC BUT, Brno University of Technology, 61200 Brno, Czech Republic. [7]INNOVENT e.V. Technologieentwicklung, 07745 Jena, Germany. [8]Institute for Theoretical Physics, Vienna University of Technology, 1040 Vienna, Austria. [9]Department of Physics and Energy Science, University of Colorado Colorado Springs, Colorado Springs, CO 80918, USA. ✉e-mail: rostyslav.serha@univie.ac.at

single magnon level[16] and the first measurements of the Wigner function of a single magnon[17] were performed also using a YIG sphere as a magnetic medium. Proposals for applications in quantum computing have also emerged, in particular, the use of YIG spheres as magnonic transducers for qubits[18]. A pressing question in the quantum magnonics community is how to bring the more complex, flexible, and property-rich structures employed in classical magnonic nanodevices to the quantum regime. Two-dimensional geometries are a paramount example, for instance YIG films down to tens of nanometers thick grown on gadolinium gallium garnet (GGG) $Gd_3Ga_5O_{12}$ substrates[5–8,10,11] enable the development of nanoscale magnetic devices and circuits[1]. As the temperature decreases, the spin-wave damping in YIG/GGG increases up to tenfold due to various effects associated with impurities in YIG and parasitic influence of the paramagnetic GGG substrate[19,26–30]. Our experimental investigations of spin-wave damping agree well with the results reported in the literature (but are out of the scope of this article).

Several experimental reports have demonstrated that lowering the temperature below about 50 K in YIG/GGG shifts the ferromagnetic resonance (FMR) frequency or the frequency of propagating spin waves[25,29,31–33]. Our experimental results, discussed in this article, show the same behavior and the interpretation given by the authors in[31], agrees with our analysis. However, at the time of the study, the measurements and calculations were not performed below 4.2 K, which is particularly interesting for quantum magnonics and is the temperature regime in which GGG shows a complex magnetic phase behavior[34,35]. Additionally, the role of the strong non-uniformity of the field induced by the partially magnetized GGG was not explored, as well as the change of crystallographic anisotropy in YIG with decreasing temperature.

Here, through experiments, theory, and numerical simulations, we studied the stray field induced by the GGG substrate at temperatures as low as 30 mK. Using vibrating-sample magnetometry (VSM), we measured the magnetization of GGG as a function of the applied field and temperature down to 1.8 K. To extrapolate values for lower temperatures, we used the Brillouin function. We utilized analytical theory and numerical simulations to determine the GGG stray field and the cubic and uniaxial crystallographic anisotropies of YIG. Our findings revealed that the GGG field is strongly nonuniform, ranging from 12 mT to 60 mT for the YIG/GGG sample with an area of (5×5) mm^2, at a temperature of 1.8 K, and an applied magnetic field of 600 mT when the magnetization of GGG was 253 kA/m. It has been experimentally confirmed by FMR measurements that the magnetization of the GGG substrate does not change with temperature below 500 mK[35] in contrast to the Brillouin model of a paramagnet. The results give access to the properties of propagating magnons in YIG/GGG at millikelvin temperatures, essential for the future of nanoscale quantum-magnonic circuits.

Results and discussion

To simulate the strength and profile of the stray field induced by the paramagnetic substrate over the YIG layer, we first measured the magnetization of a bare GGG substrate, as shown in Fig. 2a. In the partially magnetized state, GGG has a small value of magnetic susceptibility $\chi \approx 0.3$ and creates a highly inhomogeneous y-field component B_{GGG}^y on its surface, as seen in Fig. 1b. As an example, at 1.8 K, this induced field B_{GGG}^y opposes the external magnetic field of 600 mT. It varies in strength from 12 mT at the center to 60 mT at the edges, antiparallel to the direction of the external magnetic field. This field is crucial in investigating YIG/GGG systems at low temperatures.

Figure 2b displays two spectra that exemplify the impact of cryogenic temperatures on the FMR signal of the YIG film in an external magnetic field of 425 mT. The FMR peak is almost entirely Lorentzian-shaped at room temperature. However, when the temperature decreases below 100 K, the peak becomes asymmetric on one side, as shown in Fig. 2b for 52 K, and then broadens significantly with a lower resonance frequency, as demonstrated for 2 K. Additionally, the amplitude of the FMR peak decreases as the temperature reduces.

Figure 2c clearly shows the impact of the stray field induced by the GGG substrate. The graph displays the FMR frequencies f_{FMR} obtained for the YIG film at various temperatures, ranging from 300 K to 30 mK. As the
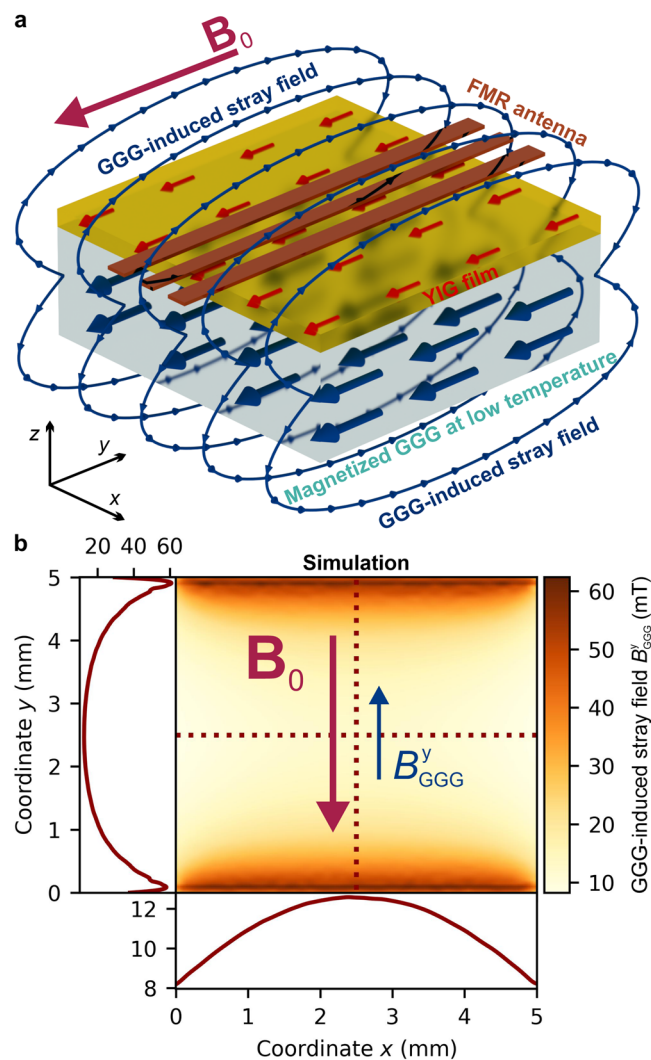
Fig. 1 | GGG-induced magnetic stray field. a Depiction of the experimental system of a YIG film grown on GGG. The sample is in-plane magnetized by an external magnetic field, and at temperatures approaching 0 K the paramagnetic GGG spin system saturates. The substrate creates an inhomogeneous stray field, that becomes an additional component to the internal magnetic field of the YIG but is oriented antiparallel to the external field. To measure FMR the YIG film sample is placed on a CPW antenna, through which the magnetic system is excited. **b** Simulation of the highly inhomogeneous B_{GGG}^y stray field y-component at the interface between YIG and GGG layers. The inhomogeneity can also be seen for the x and y-axis for the center of the sample by the two cross-section plots marked in the 2D map with the red dotted lines. The simulation is performed using a non-linear Maxwell solver[47] for the temperature 1.8 K and the strength of the applied external magnetic field of 600 mT at which the magnetization of GGG was 253 kA/m.

temperature decreases, the FMR frequency increases due to the rise in the saturation magnetization of YIG. The theoretical curves, represented by dashed lines, were calculated using Eq. (4), with the gyromagnetic ratio γ and effective anisotropy field B_{ani}^{eff} taken from the Kittel fit at room temperature, but neglecting the contribution of the GGG-induced stray field ($B_{GGG} = 0$). The theoretically expected FMR frequency saturates at temperatures below 50 K.

At temperatures below 50 K, the experimental FMR frequencies deviate from the theoretical values due to the GGG-induced stray field. The data indicate that for an external field B_0 of 925 mT, the FMR frequency begins to decrease at approximately 50 K, while for B_0 values of 325 mT, this occurs at around 25 K. At temperatures below 2 K and high external fields of 925 mT, there is a notable deviation of over 0.5 GHz between the experimental and theoretical results. This difference is attributed to the GGG stray
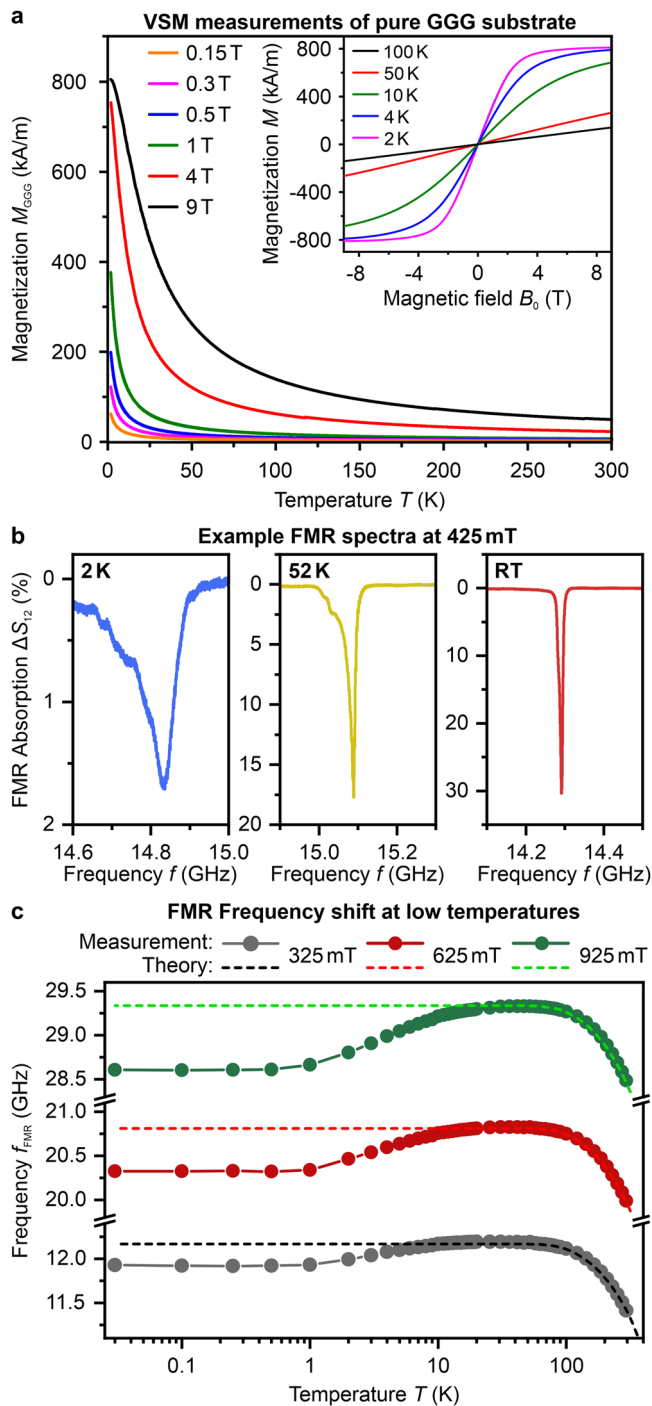
Fig. 2 | VSM and FMR measurements. a VSM measurements of the magnetization of GGG M_{GGG} as a function of the temperature T and the external magnetic field B_0. The used sample is a $(3 \times 3 \times 0.5)$ mm^3 monocrystaline GGG slab, magnetized along one of the long axes. M_{GGG} saturates at a value of 805 kA/m. The graphs represent the GGG magnetization over the range available in the experiment. **b** Example spectra of FMR at the temperatures of 2 K, 52 K, and room temperature (RT) for an external magnetic field of 425 mT. **c** FMR frequency as function over the temperature, plotted in a x-axis logarithmic scale, for three different magnetic fields. Measurements are depicted as points and were performed with the sample magnetized in the $\langle 1\bar{1}0 \rangle$ direction. The dotted lines are portraying the analytical calculation for the frequency of the FMR by the Kittel formula (Eq. (4)), which is neglecting the induced GGG stray field ($B_{\text{GGG}} = 0$). The theoretical values for M^s_{YIG} are taken from[44]. The parameters for the gyromagnetic ratio γ and effective anisotropy field $B^{\text{eff}}_{\text{ani}}$ are obtained by fitting room temperature measurements.

field, which opposes the external magnetic field and lowers the FMR frequency f_{FMR} of YIG. The FMR frequency shift, dependent on M_{GGG}, becomes more pronounced as the temperature decreases and the external magnetic field increases, as shown in Fig. 2c. The results of comparing three different magnetic fields at 30 mK shows that the impact is more pronounced at higher excitation frequencies, which is associated with stronger magnetic fields.

Below 500 mK, the frequency f_{FMR} displays unusual behavior as its decline stabilizes, showing negligible change down to 30 mK, despite the varied magnetization of GGG in this temperature range as predicted by the Brillouin function (Eq. (6)). This phenomenon is due to the complex nature of GGG, which possesses a geometrically highly frustrated spin system[36,37], leading to a complex phase diagram for temperatures below 1 K[34,35]. Understanding the sub-kelvin temperature behavior of GGG requires considering competing interactions among loops of spins, trimers, and decagons, along with the interplay between antiferromagnetic, incommensurate, and ferromagnetic orders[35]. Consequently, the Brillouin function fails to describe the magnetization of GGG below 500 mK and can be seen even clearer in later described Fig. 3c. This finding aligns with previous experimental studies[35] using different techniques, such as single-crystal magnetometry and polarized neutron diffraction. Both a single crystal and a powder GGG sample were investigated in this study and showed the same behavior.

Incorporating the analytically calculated GGG stray field B_{GGG} into the Kittel formula Eq. (4) is necessary for determining the FMR frequency. To accurately identify the FMR frequencies f_{FMR}, e.g. shown in Fig. 2b, it is essential to account for the GGG-induced stray field B_{GGG} at the sample center. At this location, the gradient is zero, and the region of the same field magnitude is the largest, most significantly affecting the area excited by the microwave stripline and determining the position of the FMR peak. The red vertical dashed line in Fig. 1b approximately depicts the position of the microstrip FMR antenna. Once incorporated into the Kittel equation, the gyromagnetic ratio γ and the effective anisotropy field $B^{\text{eff}}_{\text{ani}}$ become fitting parameters. Obtaining $B^{\text{eff}}_{\text{ani}}$ allows us to gain insight into and make predictions about the internal field of thin YIG films at low temperatures. Figure 3a displays the fitting outcomes for the magnetization orientations of $\langle 1\bar{1}0 \rangle$ (red) and $\langle 11\bar{2} \rangle$ (black), with the effective anisotropy field $B^{\text{eff}}_{\text{ani}}$ plotted against temperature, with the x-axis in a logarithmic scale. The error bars are taken from the root-mean-square deviation of the fit. At room temperature, the anisotropy field is relatively small, measuring approximately 5 mT, with a variation of about 0.6 mT between the two orientations due to the cubic anisotropy of the YIG single crystal.

However, as the temperature decreases, both the strength of $B^{\text{eff}}_{\text{ani}}$ and the difference between $\langle 1\bar{1}0 \rangle$ and $\langle 11\bar{2} \rangle$ magnetization directions increase significantly. At a temperature of 2 K, the effective anisotropy field $B^{\text{eff}}_{\text{ani}}$ is more than 3.2 and 3.5 times larger for the $\langle 1\bar{1}0 \rangle$ and $\langle 11\bar{2} \rangle$ directions, respectively, than at room temperature. The inset in Fig. 3a displays the second fitting parameter, the gyromagnetic ratio γ, as a function of temperature on a x-axis logarithmic scale. It is known from previous research on YIG that γ is considered to be weakly temperature dependent[30,38,39]. The behavior of γ shows a very weak decrease at lower temperatures, changing from 28.13 GHz/T to 28.02 GHz/T. γ is nearly identical for both magnetization directions, and the values fall within each other's error bars.

To get a better understanding of the changes in the effective anisotropy field $B^{\text{eff}}_{\text{ani}}$, the field was divided into its two main components: the cubic anisotropy field B_c and the uniaxial anisotropy field B_u. This separation is achieved by considering the two magnetization directions and applying two separate equations for the FMR frequency, as described in[40].

$$f^{\langle 1\bar{1}0 \rangle}_{\text{FMR}} = \gamma^{\langle 1\bar{1}0 \rangle} \cdot \sqrt{(B_0 - B_{\text{GGG}}) \cdot (B_0 - B_{\text{GGG}} - B_u - B_c + \mu_0 M_s) - 2B_c^2}, \tag{1}$$

$$f^{\langle 11\bar{2} \rangle}_{\text{FMR}} = \gamma^{\langle 11\bar{2} \rangle} \cdot \sqrt{(B_0 - B_{\text{GGG}}) \cdot (B_0 - B_{\text{GGG}} - B_u - B_c + \mu_0 M_s)}. \tag{2}$$

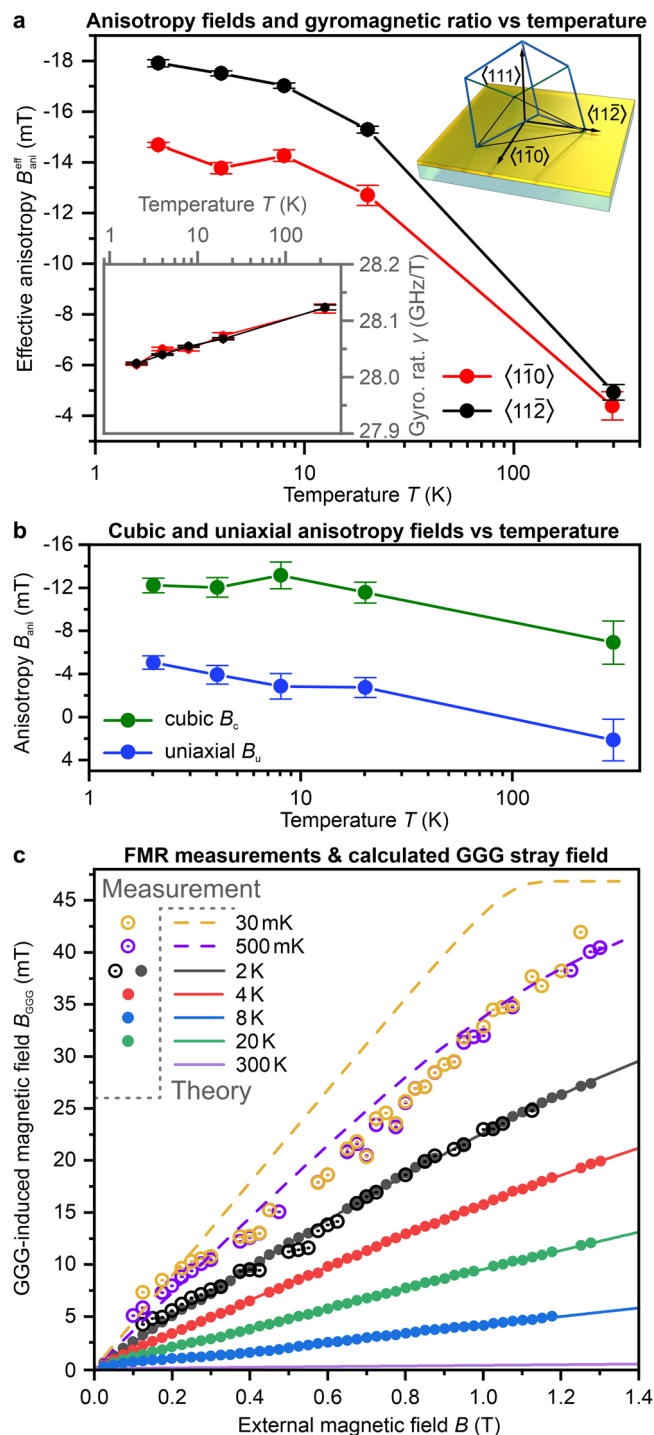**Fig. 3 | Crystallographic anisotropies and magnitude of GGG-induced stray field.**
a Effective anisotropy field B_{ani}^{eff} of the YIG film as a function of the temperature in a
x-axis logarithmic scale for two different crystallographic magnetization directions
— $\langle 1\bar{1}0 \rangle$ and $\langle 11\bar{2} \rangle$, schematically shown by the inset in the right corner. The inset in
the left corner depicts the gyromagnetic ratio γ as a function of the temperature for
the same magnetization geometries respectively. The points are obtained as fitting
parameters from Eq. (4). **b** Cubic and uniaxial anisotropiy fields B_c, B_u vs tem-
perature T. Values for B_c and B_u were obtained from according Eq. (1) and (2) for the
Kittel fits[40]. **c** GGG-induced stray field in YIG film center as a function of the
externally applied magnetic field B_0. Solid lines are the values calculated from the
measured M_{GGG} by Eq. (5) of the VSM and solid lines are values calculated from the
FMR peaks measured in the PPMS by converting Eq. (4) for B_{GGG}. The hollow points
are B_{GGG} values calculated from FMR peak measurements performed in the dilution
refrigerator. The dotted lines are calculated via Eq. (5) by taking the extrapolated
values of M_{GGG} by the Fit from Eq. (6).

Using Eq. (1) and Eq. (2) to fit the FMR frequency f_{FMR} data, and utilizing
the gamma values from Fig. 3a, we can obtain values for the two distinct
anisotropy fields, B_c (green) and B_u (blue) and their errors by root-mean-
square deviation. The resulting plot in Fig. 3b shows the anisotropy field B_{ani}
as a function of temperature T on a x-axis logarithmic scale. Our
experimental findings at room temperature indicate (-6.9 ± 2) mT for B_c
and (2.1 ± 2) mT for B_u, which agree well with previously reported values for
thin YIG films[6]. Notably, the cubic anisotropy increases to (-12.2 ± 0.8) mT
at temperatures as low as 2 K, almost doubling the room temperature value.
The uniaxial anisotropy exhibits a unique characteristic of changing its
positive-to-negative sign at cryogenic temperatures and reaching a peak
value of (-5.1 ± 0.7) mT at 2 K.

With this understanding of the low-temperature anisotropy and the
stray field caused by GGG, we can make accurate predictions about the FMR
behavior in YIG films even at temperatures as low as 2 K. Note, that the
anisotropy increase reaches a saturation point below 10 K, as demonstrated
in Fig. 3a. As a result, we can assume that the anisotropy remains constant
down to the millikelvin temperatures and can be treated as equivalent to the
2 K values.

However, in the absence of magnetization M_{GGG} measurements below
2 K, we cannot utilize experimental data to compute the stray field B_{GGG}
using Eq. (5). Therefore, we must rely on the Brillouin fit presented in Sec.
III-A (Eq. (6)) and extrapolate M_{GGG} as an estimation. Additionally, a
second method was used to determine the values for B_{GGG} at millikelvin
temperatures in the center of the YIG sample by measuring the FMR
position at these temperatures and rearranging Eq. (4) to solve for B_{GGG}.

The results are shown in Fig. 3c. It depicts the stray field induced by
GGG at the center of the sample as a function of the externally applied
magnetic field B_0. The solid lines represent the calculated values of B_{GGG} for
temperatures of 2 K and above, while the solid points represent the obtained
B_{GGG} from the FMR measurements. Both data sets match perfectly. This
alignment, in Eq. (4), highlights the accuracy of the fitted effective aniso-
tropy B_{ani}^{eff}, affirming the precision and appropriateness of the fit. The data
points shown by the hollow-center-dot illustrate the B_{GGG} values acquired
via FMR measurements in the dilution refrigerator, spanning a temperature
range of 30 mK to 2 K. It is worth noting that the values of B_{GGG} at 2 K
obtained from both the dilution refrigerator and the PPMS measurements
are consistent.

The measurements within the dilution refrigerator exhibited a lower
signal-to-noise ratio, which led to a higher scattering of the data points in
Fig. 3c. At temperatures of 2 K, 500 mK, and 30 mK, it was necessary to
maintain the applied power at a low level (below -25 dBm) to ensure that the
system remained in thermal equilibrium, which resulted in a more noisy
signal. This more noisy signal, together with the asymmetry of the FMR
signal (see Fig. 2b at 2 K), increased the uncertainty of the FMR frequency fit
(see Methods below).

The extrapolated data obtained through the Brillouin fit is shown as
dotted lines for both 500 mK and 30 mK, in comparison to the experimental
data (Fig. 3c). At 500 mK, the extrapolation matches at fields above 1 T and
below 300 mT with the experimental data but diverts in between (purple
circle points and dashed line). At 30 mK, it does not match (yellow circle
points and dashed line). The extrapolated field strength of GGG (dashed
yellow) experiences a sharp increase and then saturates above 1.1 T. While
the extrapolated curves deviate, the measured data for 30 mK and 500 mK
overlap. These results show that the method of fitting the GGG magneti-
zation M_{GGG} and the stray magnetic field B_{GGG} effectively describes the
inter- and extrapolations only at temperatures above 500 mK. This lim-
itation confirms the conclusion above. M_{GGG} is solely dependent on the
externally applied magnetic field below 500 mK, which is supported by the
behavior of the FMR frequency in Fig. 2c and previous research on the
complex behavior of GGG phase states[35]. At these temperatures, GGG was
observed to transition through various magnetic phases, such as spin glass
and antiferromagnetic, depending on the external magnetic field[34].

To conclude, our findings demonstrate that YIG films grown on GGG
substrates are impacted by stray fields originating from the partially

magnetized paramagnetic GGG at low temperatures and under externally applied magnetic fields. The strength and configuration of these fields depend on the shape of the GGG substrate (the ratio between the width, length and thickness of the sample) and are highly inhomogeneous across the YIG layer. In the in-plane magnetization geometry, the stray field can reach up to 40 mT in the center and increases five-fold at the edges of the sample. Taking into account this geometrical behavior, one can change the shape of the substrate and thus keep the magnetic field homogeneous over the surface area, for example, in quantum-magnonic circuits based on YIG/GGG structures.

We used an analytical approach validated by micromagnetic simulations to calculate the stray field B_{GGG} induced by GGG. This approach allowed us to integrate B_{GGG} into the Kittel-fit formula and accurately determine the effective anisotropy field B_{ani}^{eff} in the crystallographic directions $\langle 1\bar{1}0 \rangle$ and $\langle 11\bar{2} \rangle$ of the YIG film for temperatures as low as 2 K. Moreover, we were able to extract the crystallographic cubic and uniaxial anisotropy fields, B_c and B_u, respectively. These fields increase in magnitude from −6.9 mT and 2.1 mT at room temperature to −12.2 mT and −5.1 mT at 2 K.

The anomalous behavior of the FMR frequency of YIG, which is constant for temperatures below 500 mK, can be explained by the absence of the variation of the GGG magnetization M_{GGG} with decreasing temperature, and therefore by the GGG-induced magnetic field B_{GGG}. This behavior can be described by the property of GGG as a geometrically highly frustrated magnet, resulting in the complex phase transition diagram of GGG at these temperatures and fields[34–37]. Our results allow accurate predictions of the YIG/GGG magnetic behavior at low and ultralow temperatures, a key element for successfully implementing future YIG/GGG quantum-magnonic networks. Additionally, the phenomena generally apply to any magnetic thin film grown on any paramagnetic substrate at low temperatures in the presence of a magnetic field.

Methods
Experimental methods
In our research, we studied a (5×5) mm^2 and 97 nm-thick YIG film grown on a 500 μm-thick GGG substrate, using liquid phase epitaxy[5,6]. We conducted stripline ferromagnetic-resonance (FMR) spectroscopy using a vector network analyzer (VNA), within a Physical Property Measurement System (PPMS), at temperatures ranging from 2 K to 300 K and up to 40 GHz. The sample was mounted on a frequency-broadband stripline and placed in a homogeneous magnetic field of up to 1.3 T created by superconducting coils. The maximum applied microwave power in the PPMS was -5 dBm. Ultralow temperature measurements were performed in a dilution refrigerator, reaching base temperatures below 10 mK. At 20 mK, the cooling power is 14 μW, sufficient to keep the system in thermal equilibrium during the FMR spectroscopy measurements at -25 dBm applied power.

The following measurements were taken with the external magnetic field in the in-plane orientation and applied along the FMR stripline antenna. To determine the FMR spectrum for a specific field, S_{12} and S_{21} parameters were measured using a VNA not only at the target field but also at reference fields adjusted to approximately 15 mT to 40 mT, both above and below the desired value[41]. By subtracting the averaged signals of the reference fields from the measured FMR signal, we obtained the FMR absorption spectrum in YIG that was not affected by GGG (see Fig. 2b as an example). This dual reference measurement approach enabled to obtain the best results when working with kelvin and sub-kelvin temperatures, since the GGG parasitic signal is greatly affected by the change in the applied field. To obtain the resonance frequency and full linewidth at half maximum, the background is first analyzed using a 1D cubic spline model[42]. The resonance shape is then fitted using the double Lorentzian model, which individually describes the left and right sides of the asymmetric absorption peaks.

To accurately determine the magnetization of GGG for our analytical calculations and numerical simulations, we utilized vibrating-sample magnetometry (VSM) on a pure GGG slab $(3 \times 3 \times 0.5)$ mm^3 in the temperature range from 1.8 K to 300 K. The raw measurement VSM data is

dependent on the sample shape due to self-demagnetization. Shape-independent values of the magnetization of GGG were extracted by calculating the internal magnetic fields B_{int} by

$$B_{int} = B_0 - \mu_0 M_{GGG} \cdot N_0, \tag{3}$$

where B_0 is the externally applied magnetic field, M_{GGG} the measured magnetization and N_0 the demagnetization factor corresponding to the magnetization direction. The Gd^{+3} ions in GGG have a relatively large spin (S = 7/2), resulting in a saturation magnetization that is notably higher than that of YIG. Specifically, the saturation magnetization of GGG, denoted by M_{GGG}^s, is equal to 805 kA/m, as shown in Fig. 2a.

Based on established practices, experimental FMR data can be used to extract the effective magnetization, the anisotropy fields, and the Gilbert damping parameter of a magnetic material (see ref. 43 and the supplementary materials therein). In this study, the temperature-dependent saturation magnetization of YIG, M_{YIG}^s, is taken from the analytical calculation performed in[44]. Thus, we can use this information to more accurately determine the anisotropy fields of YIG using them as a fitting parameter.

As reported in the literature[19,31] and supported by our FMR analysis, the paramagnetic GGG becomes sufficiently magnetized at temperatures below about 100 K, together with an external magnetic field applied. This magnetization induces a magnetic stray field B_{GGG} in the YIG layer, which causes a shift of the YIG FMR frequencies[31]. For the in-plane applied magnetic field, the FMR shift is toward lower frequencies because B_{GGG} and the applied bias field B_0 are antiparallel. Conversely, in an out-of-plane geometry, the stray field B_{GGG} aligns parallel to the field B_0, resulting in a shift of the resonance frequency to higher values[31]. The positive shift was also confirmed by our experimental results, but in this paper, we focus only on the in-plane configuration.

The magnitude of this inhomogeneous stray field B_{GGG} is influenced by both the temperature and the strength of the external magnetic field. At lower temperatures and higher external fields, the GGG-induced stray field becomes more pronounced, which is crucial for determining the FMR frequency f_{FMR}. The modified Kittel formula tailored for in-plane magnetization geometry describes the influence of this field on the FMR frequency:

$$f_{FMR} = \gamma \cdot \sqrt{(B_0 - B_{GGG}) \cdot (B_0 - B_{GGG} + B_{ani}^{eff} + \mu_0 M_{YIG}^s)}, \tag{4}$$

where γ is the reduced gyromagnetic ratio, B_0 is the applied external field, B_{ani}^{eff} the effective crystallographic anisotropy field[43], which is a fit parameter as described in detail below, B_{GGG} is the GGG-induced stray field defined analytically in the next section and M_{YIG}^s the theoretical value for the saturation magnetization of YIG at any temperature taken from[44].

Analytical calculation of GGG field
At low temperatures below 10 K and in the presence of magnetic fields measuring several hundred millitesla, GGG attains a significant magnetization exceeding hundreds of kA/m (see Fig. 2a). In this state, the GGG substrate becomes a magnet and emits a stray magnetic field that expands beyond its volume. To accurately determine the strength and characteristics of the stray field generated by the GGG, two crucial parameters are required: M_{GGG}, which denotes the magnetization of GGG, and $\tilde{N}_{xx}$, which represents the averaged mutual in-plane demagnetization factor of GGG and YIG layers. Then, one can accurately determine the strength and characteristics of the stray field generated by the GGG in the direction of the external field B_{GGG} as

$$B_{GGG} = \mu_0 M_{GGG}(T, B_0) \tilde{N}_{xx}. \tag{5}$$

B_{GGG} is crucial for understanding its overall magnetic influence, particularly at low temperatures, on the internal field of the YIG film. Net GGG

magnetization M_{GGG} is given by the implicit equation[45]:

$$M_{GGG} = M_{GGG}^s \cdot \mathscr{B}_{\frac{7}{2}}\left(\frac{7}{2} \cdot \frac{g\,\mu_B \cdot (B_0 - \mu_0\,M_{GGG}\,N_{xx} + \lambda\,\mu_0\,M_{GGG})}{k_B\,T}\right),$$

(6)

where $M_{GGG}^s = 805$ kA/m denotes the saturation magnetization of GGG, $g = 2$ the Landé factor, μ_B the Bohr magneton, $\mathscr{B}_{\frac{7}{2}}$ the Brillouin function for the angular momentum $J = \frac{7}{2}$, λ the coefficient of the molecular field and N_{xx} is the standard demagnetization factor (i.e. self-demagnetization) of the YIG/GGG sample.

In our case of a thin GGG cuboid of the sizes $2a \times 2a \times 2c$, where $c \ll a$, the self-demagnetization factor can be approximated as[46]

$$N_{xx} \approx \frac{c}{\pi a}\left(0.726 - \log\frac{c}{a}\right).$$

(7)

For the mutual demagnetization factor, we account that the YIG film is much thinner than the GGG substrate, and that we deal with nonuniform FMR in YIG, because the lateral sizes of YIG are much larger than the spin-wave free path, so that standing eigenmodes are not formed. In this case, the FMR peak position is mostly determined by the central YIG area, for which the mutual demagnetization factor is

$$\tilde{N}_{xx} = \frac{1}{\pi} \cdot \arctan\left[\frac{\sqrt{2}c}{\sqrt{a^2 + 2c^2}}\right].$$

(8)

Full expressions for arbitrary prisms are available in[46]. Note, both approximations for self and mutual demagnetization factors may not be adequate for small external fields B_0, as it neglects the potential nonuniform magnetization of GGG.

To ensure that our calculations and numerical micromagnetic simulations would be most precise, the magnetization of GGG M_{GGG} was measured for each temperature within the same field range used in the FMR experiments. For calculations at temperatures below 1.8 K, we relied on the VSM data obtained earlier. The data was fitted using Eq. (6) by adjusting the molecular field $\lambda = -0.854$ and saturation magnetization $M_{GGG}^s = 831$ kA/m as fitting parameters. This fitting method was used to extrapolate the values of M_{GGG} with respect to temperature T and external magnetic field B_0. It allowed us to compare our theoretical and simulation work with experimental results even at temperatures below 1.8 K.

Numerical simulations
To gain a better understanding of the magnetic stray field present in the YIG layer on the GGG substrate, we performed numerical simulations that provide a more precise representation of the field inhomogeneity compared to analytical calculations. To simulate the induced stray field in YIG, we solved the magnetostatic Maxwell equations within the GGG layer with a nonlinear material law (e.g. magnetization curves Fig. 2a inset) extracted from the VSM measurements at $T = 1.8$ K. For the simulation a finite element/boundary element method is used with a mesh size of 0.1 mm[47]. The field is evaluated 50 nm above the GGG surface as a projection to the external applied in-plane bias field B_0, as depicted in Fig. 1b.

References
1. Chumak, A. V. et al. Advances in magnetics roadmap on spin-wave computing. *IEEE Trans. Magn.* **58**, 1–72 (2022).
2. Dillon, J. F. Ferrimagnetic resonance in yttrium iron garnet. *Phys. Rev.* **105**, 759–760 (1957).
3. LeCraw, R. C., Spencer, E. G. & Porter, C. S. Ferromagnetic resonance line width in yttrium iron garnet single crystals. *Phys. Rev.* **110**, 1311–1313 (1958).
4. Klingler, S. et al. Gilbert damping of magnetostatic modes in a yttrium iron garnet sphere. *Appl. Phys. Lett.* **110**, 092409 (2017).
5. Dubs, C. et al. Sub-micrometer yttrium iron garnet LPE films with low ferromagnetic resonance losses. *J. Phys. D: Appl. Phys.* **50**, 204005 (2017).
6. Dubs, C. et al. Low damping and microstructural perfection of sub-40nm-thin yttrium iron garnet films grown by liquid phase epitaxy. *Phys. Rev. Mater.* **4**, 024416 (2020).
7. Ding, J., Liu, T., Chang, H. & Wu, M. Sputtering growth of low-damping yttrium-iron-garnet thin films. *IEEE Magn. Lett.* **11**, 1–5 (2020).
8. Heyroth, F. et al. Monocrystalline freestanding three-dimensional yttrium-iron-garnet magnon nanoresonators. *Phys. Rev. Appl.* **12**, 054031 (2019).
9. Cornelissen, L. J., Liu, J., Duine, R. A., Youssef, J. B. & van Wees, B. J. Long-distance transport of magnon spin information in a magnetic insulator at room temperature. *Nature Physics* **11**, 1022–1026 (2015).
10. Onbasli, M. C. et al. Pulsed laser deposition of epitaxial yttrium iron garnet films with low gilbert damping and bulk-like magnetization. *APL Mater.* **2**, 106102 (2014).
11. Hahn, C. et al. Measurement of the intrinsic damping constant in individual nanodisks of Y$_3$Fe$_5$O$_{12}$|Pt. *Appl. Phys. Lett.* **104**, 152410 (2014).
12. Cherepanov, V., Kolokolov, I. & L'vov, V. The saga of yig: Spectra, thermodynamics, interaction and relaxation of magnons in a complex magnet. *Physics Reports* **229**, 81–144 (1993).
13. Borst, M. et al. Observation and control of hybrid spin-wave-meissner-current transport modes. *Science* **382**, 430–434 (2023).
14. Awschalom, D. D. et al. Quantum engineering with hybrid magnonic systems and materials (invited paper). *IEEE trans. quantum eng.* **2**, 1–36 (2021).
15. Lachance-Quirion, D., Tabuchi, Y., Gloppe, A., Usami, K. & Nakamura, Y. Hybrid quantum systems based on magnonics. *Appl. Phys. Express* **12**, 070101 (2019).
16. Lachance-Quirion, D. et al. Entanglement-based single-shot detection of a single magnon with a superconducting qubit. *Science* **367**, 425–428 (2020).
17. Xu, D. et al. Quantum control of a single magnon in a macroscopic spin system. *Phys. Rev. Lett.* **130**, 193603 (2023).
18. Li, Y. et al. Hybrid magnonics: Physics, circuits, and applications for coherent information processing. *J. Appl. Phys.* **128**, 130902 (2020).
19. Knauer, S. et al. Propagating spin-wave spectroscopy in a liquid-phase epitaxial nanometer-thick YIG film at millikelvin temperatures. *J. Appl. Phys.* **133**, 143905 (2023).
20. Yuan, H., Cao, Y., Kamra, A., Duine, R. A. & Yan, P. Quantum magnonics: When magnon spintronics meets quantum information science. *Phys. Rep.* **965**, 1–74 (2022).
21. Zare Rameshti, B. et al. Cavity magnonics. *Phys. Rep.* **979**, 1–61 (2022).
22. Li, Y. et al. Coherent coupling of two remote magnonic resonators mediated by superconducting circuits. *Phys. Rev. Lett.* **128**, 047701 (2022).
23. Morris, R., Van Loo, A., Kosen, S. & Karenowska, A. Strong coupling of magnons in a YIG sphere to photons in a planar superconducting resonator in the quantum limit. *Sci. Rep.* **7**, 11511 (2017).
24. Van Loo, A., Morris, R. & Karenowska, A. Time-resolved measurements of surface spin-wave pulses at millikelvin temperatures. *Phys. Rev. Appl.* **10**, 044070 (2018).
25. Karenowska, A. D., Patterson, A. D., Peterer, M. J., Magnússon, E. B. & Leek, P. J. Excitation and detection of propagating spin waves at the single magnon level. *arXiv preprint arXiv:1502.06263* (2015).
26. Jermain, C. L. et al. Increased low-temperature damping in yttrium iron garnet thin films. *Phys. Rev. B* **95**, 174411 (2017).

27. Mihalceanu, L. et al. Temperature-dependent relaxation of dipole-exchange magnons in yttrium iron garnet films. *Phys. Rev. B* **97**, 214405 (2018).

28. Kosen, S., van Loo, A. F., Bozhko, D. A., Mihalceanu, L. & Karenowska, A. D. Microwave magnon damping in YIG films at millikelvin temperatures. *APL Mater.* **7**, 101120 (2019).

29. Guo, S., McCullian, B., Hammel, P. C. & Yang, F. Low damping at few-k temperatures in $Y_3Fe_5O_{12}$ epitaxial films isolated from $Gd_3Ga_5O_{12}$ substrate using a diamagnetic $Y_3Sc_{2.5}Al_{2.5}O_{12}$ spacer. *J. Magn. Magn. Mater.* **562**, 169795 (2022).

30. Will-Cole, A. R. et al. Negligible magnetic losses at low temperatures in liquid phase epitaxy grown $Y_3Fe_5O_{12}$ films. *Phys. Rev. Mater.* **7**, 054411 (2023).

31. Danilov, V., Lyfar', D., Lyubon'ko, Y. V., Nechiporuk, A. Y. & Ryabchenko, S. Low-temperature ferromagnetic resonance in epitaxial garnet films on paramagnetic substrates. *Soviet Physics Journal* **32**, 276–280 (1989).

32. Wang, L. et al. Magnetization coupling in a YIG/GGG structure. *Phys. Rev. B* **102**, 144428 (2020).

33. Roos, M. J. et al. Magnetization and antiferromagnetic coupling of the interface between a 20 nm $Y_3Fe_5O_{12}$ film and $Gd_3Ga_5O_{12}$ substrate. *Phys. Rev. Mater.* **6**, 034401 (2022).

34. Petrenko, O. A., Ritter, C., Yethiraj, M. & McK Paul, D. Investigation of the low-temperature spin-liquid behavior of the frustrated magnet gadolinium gallium garnet. *Phys. Rev. Lett.* **80**, 4570–4573 (1998).

35. Deen, P. P., Florea, O., Lhotel, E. & Jacobsen, H. Updating the phase diagram of the archetypal frustrated magnet $Gd_3Ga_5O_{12}$. *Phys. Rev. B* **91**, 014419 (2015).

36. Schiffer, P., Ramirez, A. P., Huse, D. A. & Valentino, A. J. Investigation of the field induced antiferromagnetic phase transition in the frustrated magnet: Gadolinium gallium garnet. *Phys. Rev. Lett.* **73**, 2500–2503 (1994).

37. Tsui, Y. K., Kalechofsky, N., Burns, C. A. & Schiffer, P. Study of the low temperature thermal properties of the geometrically frustrated magnet: Gadolinium gallium garnet. *J. Appl. Phys.* **85**, 4512–4514 (1999).

38. Haidar, M. et al. Thickness- and temperature-dependent magnetodynamic properties of yttrium iron garnet thin films. *J. Appl. Phys.* **117**, 17D119 (2015).

39. Maier-Flaig, H. et al. Temperature-dependent magnetic damping of yttrium iron garnet spheres. *Phys. Rev. B* **95**, 214423 (2017).

40. Bobkov, V. B. & Zavislyak, I. V. Equilibrium state and magnetic permeability tensor of the epitaxial ferrite films. *Phys. Status Solidi A* **164**, 791–804 (1997).

41. Maier-Flaig, H. et al. Note: Derivative divide, a method for the analysis of broadband ferromagnetic resonance in the frequency domain. *Rev. Sci. Instrum.* **89**, 076101 (2018).

42. Herrera-Gomez, A. et al. Double lorentzian lineshape for asymmetric peaks in photoelectron spectroscopy. *J. Vac. Sci. Technol. A* **41**, 043208 (2023).

43. Böttcher, T. et al. Fast long-wavelength exchange spin waves in partially compensated Ga:YIG. *Appl. Phys. Lett.* **120**, 102401 (2022).

44. Hansen, P., Röschmann, P. & Tolksdorf, W. Saturation magnetization of gallium-substituted yttrium iron garnet. *J. Appl. Phys.* **45**, 2728–2732 (1974).

45. Barak, J., Huang, M. & Bhagat, S. Electron paramagnetic resonance study of gadolinium–gallium–garnet. *J. Appl. Phys.* **71**, 849–853 (1992).

46. Aharoni, A. Demagnetizing factors for rectangular ferromagnetic prisms. *J. Appl. Phys.* **83**, 3432–3434 (1998).

47. Bruckner, F. et al. 3D FEM-BEM-coupling method to solve magnetostatic maxwell equations. *J. Magn. Magn. Mater.* **324**, 1862–1866 (2012).

Author contributions

R.O.S. conducted all measurements, processed and analyzed the data, and authored the initial draft of the manuscript. A.A.V. executed the micromagnetic simulations, implemented the method for fitting the data, and contributed to data analysis. SA.K., C.A. and D.S. developed the software used for micromagnetic simulations. DA.S., SA.K., D.A.B. and S.K. constructed the experimental setup and supported the experimental investigations. K.O.L., K.D., Q.W. and M.U. assisted in interpreting the experimental data and provided insights into the measurement results. M.L., T.R. and C.D. synthesized the YIG film. R.V. and C.G.B. provided theoretical support. B.B. and O.V.D. facilitated support in conducting PPMS measurements. S.K. supervised the millikelvin experiments. A.V.C. led the project. All authors discussed the results and contributed to the manuscript.

Competing interests

The authors declare no competing interests.

Additional information

Correspondence and requests for materials should be addressed to Rostyslav O. Serha.

Reprints and permissions information is available at http://www.nature.com/reprints

Publisher's note Springer Nature remains neutral with regard to jurisdictional claims in published maps and institutional affiliations.